

Article

Thermal analysis, compressibility, and decomposition of synthetic bastnäsite-(La) to lanthanum oxyfluoride

Richard L. Rowland II ^{1*}, Barbara Lavina ², Kathleen E. Vander Kaaden ³, Lisa R. Danielson ⁴ Pamela C. Burnley ^{5,*}

¹ Los Alamos National Laboratory, Los Alamos, NM 87544, USA; RLRowland@LANL.Gov;

² Advanced Photon Source, Argonne National Laboratory, 9700 Cass Ave, Lemont, IL 60439; Blavina@anl.gov

³ Jacobs, NASA Johnson Space Center, Mail Code XI3, Houston, TX 77058, USA; Kathleen.E.VanderKaaden@NASA.Gov

⁴ Los Alamos National Laboratory, Los Alamos, NM 87544, USA; LDanielson@LANL.Gov;

⁵ University of Nevada Las Vegas, Las Vegas, NV 89154; Pamela.Burnley@unlv.edu

* Correspondence: rrowland@lanl.gov, Pamela.Burnley@unlv.edu

Received: December 30, 2019; Accepted: date; Published: date

Abstract: Understanding basic material properties of rare earth element (REE) bearing minerals such as their phase stability and equations of state can assist in understanding how economically viable deposits might form. Bastnäsite is the most commonly mined REE bearing mineral. We synthesized the lanthanum-fluoride end member, bastnäsite-(La) (LaCO₃F), and investigated its thermal behavior and decomposition products from 298 K to 1173 K under ambient pressure conditions through thermogravimetric analysis, differential scanning calorimetry, evolved gas analysis, and high temperature powder X-ray diffraction. We also investigated the compressibility of bastnäsite-(La) via single crystal X-ray diffraction in diamond anvil cells at ambient temperature up to 11.3 GPa and from 4.9 to 7.7 GPa up to 673 K. At ambient pressure, bastnäsite-(La) was stable up to 598 K, where it decomposed into CO₂ and tetragonal γ-LaOF. Above 948 K, cubic α-LaOF is stable. High temperature X-ray diffraction data were used to fit the Fei thermal equation of state and the thermal expansion coefficient α_{298} for all three materials. Bastnäsite-(La) was fit from 298 K to 723 K with $V_0 = 439.82 \text{ Å}^3$, $\alpha_{298} = 4.32 \times 10^{-5} \text{ K}^{-1}$, $a_0 = -1.68 \times 10^{-5} \text{ K}^{-1}$, $a_1 = 8.34 \times 10^{-8} \text{ K}^{-1}$, and $a_2 = 3.126 \text{ K}^{-1}$. Tetragonal γ-LaOF was fit from 723 K to 948 K with $V_0 = 96.51 \text{ Å}^3$, $\alpha_{298} = 2.95 \times 10^{-4} \text{ K}^{-1}$, $a_0 = -2.41 \times 10^{-5} \text{ K}^{-1}$, $a_1 = 2.42 \times 10^{-7} \text{ K}^{-1}$, and $a_2 = 41.147 \text{ K}^{-1}$. Cubic α-LaOF was fit from 973 K to 1123 K with $V_0 = 190.71 \text{ Å}^3$, $\alpha_{298} = -1.12 \times 10^{-5} \text{ K}^{-1}$, $a_0 = 2.36 \times 10^{-4} \text{ K}^{-1}$, $a_1 = -1.73 \times 10^{-7} \text{ K}^{-1}$, and $a_2 = -17.362 \text{ K}^{-1}$. An ambient temperature 3rd order Birch-Murnaghan equation of state was fit with $V_0 = 439.82 \text{ Å}^3$, $K_0 = 105 \text{ GPa}$, and $K' = 5.58$.

Keywords: Bastnäsite; Equation of State; Rare earth element

1. Introduction

Rare earth elements (REE), the elements with atomic number 57 to 71, are the first on the periodic table to begin populating f-block orbitals. Because of this, they exhibit unique electronic properties and thus are sought after for various technological applications for which other metals are not suitable. They are considered rare, not because of their relative abundance in the Earth's crust, but because they are generally only found as trace impurities instead of primary cations in minerals [1,2]. Relative crustal abundances of REEs are higher than noble metals such as gold or platinum, and some REEs are more common than base metals like lead [2,3]. The limited number of minerals that form with high REE content are rarely found in high enough concentrations to make economically viable deposits [2]. Currently, China controls >90% of the world's supply of REEs [1], presenting the potential for a supply problem. Understanding basic material properties of REE bearing minerals such as the temperatures at which different phases are thermodynamically stable and how they respond to changes in pressure and temperature can assist in understanding how economically viable deposits form.

Having the general formula of $(\text{Ce}, \text{La}, \text{Nd}, \text{Y})\text{CO}_3(\text{F}, \text{OH})$, bastnäsite is the most common mineral mined for REEs [4]. It occurs mainly in carbonatites and is usually found in association with calcite, dolomite, and barite [5–7], but also occurs in other geologic settings important for REE-bearing minerals [8]. Bastnäsite-(La) is the lanthanum fluoride end member (LaCO_3F) [2,4,9–14]. This work explores the ambient pressure thermal behavior of bastnäsite-(La) and the oxyfluorides it decomposes to using thermogravimetric analysis, differential scanning calorimetry, evolved gas analysis, and high temperature X-ray powder diffraction. We also explore the behavior of bastnäsite-(La) at high pressure via single crystal X-ray diffraction in a diamond anvil cell.

1.1 Structure and decomposition of bastnäsite-(La) to lanthanum oxyfluoride

Bastnäsite-(La) (LaCO_3F) exhibits hexagonal symmetry in the P-62c space group. Each unit cell contains six formula units of alternating layers of carbonate anions and layers of lanthanum cations and fluorine anions (Figure 1). The lanthanum-fluoride layers are parallel to the *a*-axis while the carbonate anion groups between them are locally parallel to the *c*-axis [4,9,10]. With the application of sufficient energy in the form of heat, bastnäsite-(La) decomposes via the decarbonation reaction $\text{LaCO}_3\text{F} + (\text{heat}) = \text{LaOF} + \text{CO}_2$ [7,15]. At ambient conditions, γ -LaOF exhibits tetragonal symmetry in the P4/nmm space group with two formula units per unit cell [16–20]. At high temperature, α -LaOF is stable with cubic symmetry in the Fm-3m space group with four formula units per unit cell [21–25]. β -LaOF is reported as stable at ambient pressure and temperature exhibiting rhombohedral symmetry in the R-3m space group with six formula units per unit cell [16,20,24]. This structure was not encountered during this investigation.

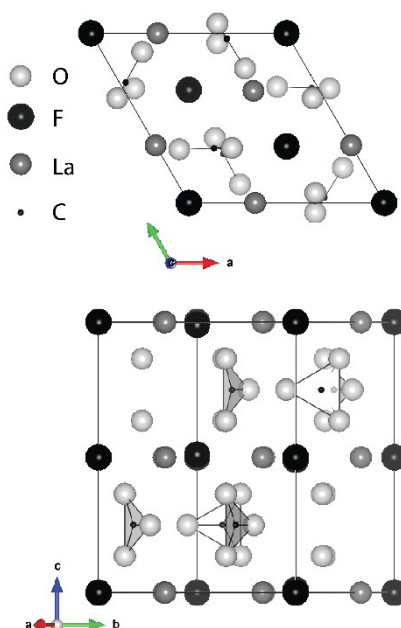


Figure 1: Structure of bastnäsite-(La) generated in the software VESTA [26], a) as viewed down the c -axis, b) as viewed down the a^* -axis [4]. In both images, the trigonal planar polyhedral for the CO_3^{2-} ions are highlighted.

2. Materials and Methods

2.1 Synthesis

Bastnäsite-(La) was synthesized via precipitation from an aqueous solution at room pressure and temperature using the method described by Janka and Schleid [15]. Aqueous solutions of each reagent were made by mixing powdered lanthanum nitrate ($\text{La}(\text{NO}_3)_3 \cdot 6\text{H}_2\text{O}$, Sigma Aldrich 203548-100G, >99% purity), sodium bicarbonate (NaHCO_3 , Sigma Aldrich S6014-25G, >99% purity), and sodium fluoride (NaF , Sigma Aldrich 201154-5G, >99% purity) with deionized water in separate beakers. The solutions were combined in a larger beaker. Bastnäsite-(La) precipitated from the mixture of solutions immediately, with sodium nitrate (NaNO_3) remaining in solution. The fluid was decanted, and the bastnäsite-(La) precipitate was washed in deionized water and centrifuged to remove residual sodium nitrate. The powder was then dried in a Fischer Scientific model 289A Isotemp Vacuum oven under vacuum at 488 K for at least 12 hours.

Phase identification was completed by powder X-ray diffraction in a PANalytical X'Pert PRO and photoacoustic infrared spectroscopy on a Digilab FTS-7000 Fourier transfer infrared (FTIR) spectrometer. Rietveld structure refinement using X'pert Highscore Plus software was used to determine that the bastnäsite-(La) starting material contained <10% LaF_3 impurity. No OH peaks were detected by FTIR between 3600 and 3400 cm^{-1} .

The powder X-ray diffraction peaks from the synthesized bastnäsite-(La) are wide due to the small particle size, so the material was next annealed in a Griggs modified piston cylinder apparatus [27] using NaCl as the pressure transmitting medium. Samples were placed in a platinum jacket, surrounded by graphite, and

sealed in a copper capsule, then subjected to pressures between 0.25 and 1.0 GPa and temperatures from 973 K to 1123 K [28]. See Figure 2 for comparison of diffraction patterns before and after annealing.

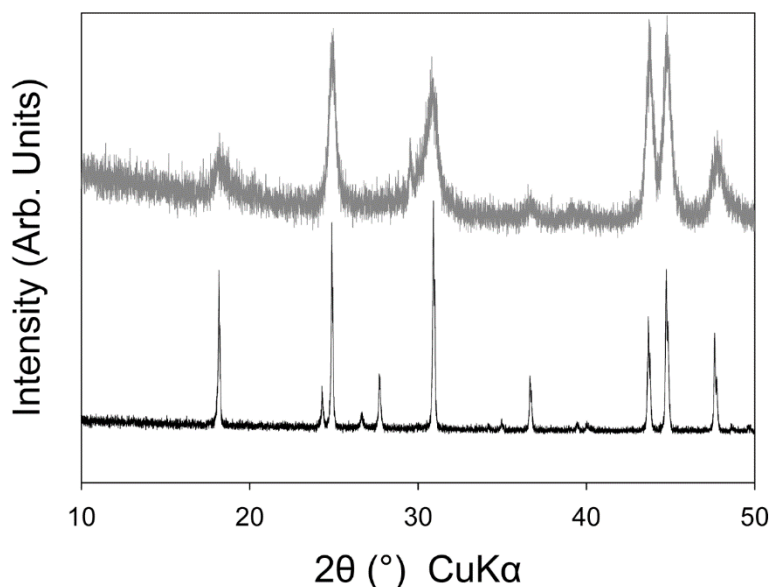


Figure 2: Powder XRD patterns of synthesized bastnäsite-(La) starting material. Top pattern is after washing and drying, bottom pattern is after annealing in the Griggs modified piston cylinder apparatus.

2.2 Thermogravimetric analysis and differential scanning calorimetry

Thermogravimetric analysis (TGA), differential scanning calorimetry (DSC), and evolved gas analysis (EGA) were used to determine the temperature at which bastnäsite-(La) begins to decompose and to determine the temperatures of phase transformations in the decomposition products. Powdered samples of at least 5 mg were heated in an alumina ceramic crucible in a Netzsch STA449 F1 Jupiter DSC/TGA apparatus under dry N₂ at 1 atm pressure at a programmed rate of 5°/min from 313 K to 1223 K. Nitrogen was used as a carrier gas because it was unreactive with the sample during heating. A second empty alumina crucible was used as the reference. It is noted that the Netzsch Jupiter DSC/TGA apparatus contains a heat-flux style calorimeter, thus exothermic reactions produce a measured increase in heat flow. A Pfeiffer Vacuum Thermostar Quadrupole mass spectrometer was used to record select masses between 1-100 AMU throughout the temperature ramp.

2.3 High temperature powder X-ray diffraction

High temperature powder X-ray diffraction was used to determine unit cell volume as a function of temperature and to determine which phases were present at different temperatures. Measurements were made in air on a PANalytical X'Pert Pro MPD Diffractometer fitted with an Anton Paar XRK 900 thermal reactor stage and an X'celerator (2.02° 2θ) detector. A cobalt X-ray source (Co Kα₁ λ=1.78901 Å) was used in angle dispersive mode from 4.0980 to 79.9814 °2θ with a step size of 0.0170° at

50.1650 seconds per step. Diffraction patterns were collected at 298 K, and in 50 degree increments from 323 K to 473 K, and in 25 degree increments from 473 K to 1173 K. A final pattern was collected at 298 K after the sample was allowed to cool. Data analysis was completed using QualX 2.0 [29], UnitCellWin64 [30] and EosFit7GUI [31].

2.4 Single crystal X-ray diffraction

In-situ single crystal synchrotron X-ray diffraction was performed at Sector 16 HPCAT of the Advanced Photon Source at Argonne National Laboratory. The pressure cells used were four-post diamond anvil cells (DAC) with 700 μm diameter culets and laser-cut rhenium gaskets with 380 μm diameter laser-cut gasket hole sample chamber [32,33]. Single crystals of the annealed bastnäsite-(La) $\sim 20\text{ }\mu\text{m}$ in diameter were placed in the sample chamber. Ruby spheres along with gold or copper powder were included in the sample chamber as pressure standards. The diamond cells were gas loaded [34] with helium, neon, or argon as the pressure transmitting media. Angle dispersive X-ray diffraction images were captured on a 2048x2048 pixel MAR CCD detector with a monochromatic beam of 30 KeV energy X-rays ($\lambda=0.3738\text{ nm}$) while rotating the DAC ± 30 degrees around the vertical axis; allowing for between 50 and 300 bastnäsite-(La) reflections to be measured. The ruby luminescence pressure scale [35] was used to estimate pressure during data collection and the equations of state for gold [36] and copper [37] were used for final pressure determination. Heated DAC experiments were conducted in a vacuum chamber with kapton and mylar windows. The DAC was equipped with resistive heating wires wound around the gasket between the anvils and around the exterior of the DAC housing to generate and maintain sample chamber temperatures up to 673 K. Thermocouples were placed in contact with the diamonds to measure the sample temperature. For the heated experiments argon was used as the pressure transmitting media, and copper (Cu) as the pressure standard. Data analysis was completed using the software packages Fit2D [38], MDI Jade (Materials Data Inc), GSE_ADA/RSV [39], and EosFit7GUI [31].

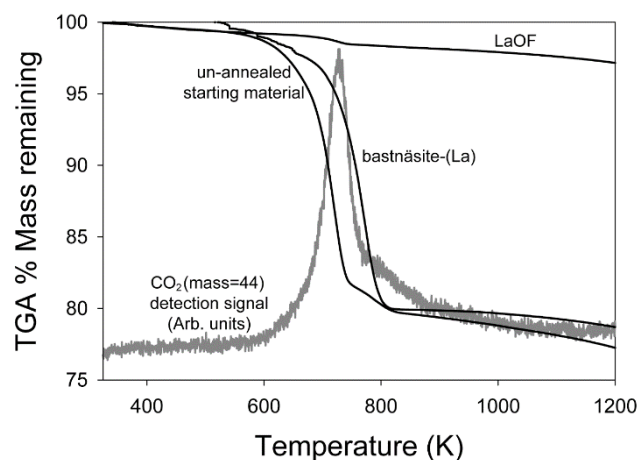
3. Results

3.1 Thermogravimetric analysis and differential scanning calorimetry

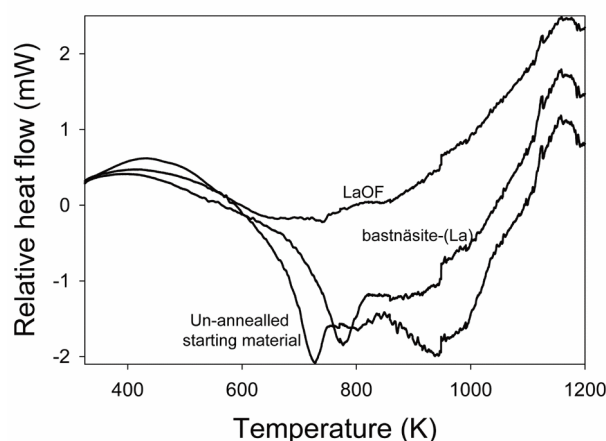
Thermogravimetric analysis and mass spectrometry CO_2 detection curves for annealed and unannealed bastnäsite-(La) and LaOF are displayed in Figure 3. Samples containing bastnäsite-(La) lost 1.0 wt. % to 1.3 wt. % between 313 K and 598 K due to adsorbed water. From 598 K to 778 K, 13.0 wt. % to 17.4 wt. % was lost due to the decomposition of bastnäsite-(La) to γ -LaOF and CO_2 . Since the LaOF sample was generated by the decomposition of bastnäsite-(La), the minor deflection of its mass loss curve at the bastnäsite-(La) decomposition point is likely caused by minor amounts of remaining bastnäsite-(La). Otherwise, the curve for LaOF does not show a significant change in slope, indicating that the LaOF itself did decompose.

The differential scanning calorimetry curves for annealed and unannealed bastnäsite-(La) (Figure 4) exhibit endotherms between 598 K and 778 K, and the mass

181 spectrometer's CO₂ detection peaked at 730 K. All samples exhibited exotherms at 948 K
 182 K and endotherms at 1123 K, indicative of phase transitions.



184 **Figure 3:** Thermogravimetric Analysis (TGA) curves for annealed bastnäsite-(La), un-
 185 annealed starting material, and LaOF from 325 K to 1223 K. CO₂ detection from the
 186 Pfeiffer Vacuum Thermostar Quadrupole mass spectrometer in light gray. Mass loss
 187 curves for the starting material and annealed bastnäsite-(La) begin to steepen at 600
 188 K, at the same time CO₂ detection begins. The mass loss curve for LaOF does not show
 189 a significant change in slope, indicating that the decomposition reaction did not occur
 190 in that sample.



192 **Figure 4:** Differential Scanning Calorimetry (DSC) curves for annealed
 193 bastnäsite-(La), un-annealed starting material, and LaOF from 325 K to 1223 K.
 194 Endotherms can be seen on both the annealed bastnäsite-(La) and un-annealed
 195 starting material curves from the range near 598 K to 773 K indicating the
 196 decomposition reaction. The LaOF curve does not exhibit this, since it did not
 197 decompose. Exotherms at 948 K and endotherms at 1123 K are evident on all three
 198 curves indicating phase transitions.

3.2 High temperature powder X-ray diffraction

Figure 5 displays a selection of the high temperature powder XRD patterns encompassing the bastnäsite-(La) decomposition reaction. Bastnäsite-(La) is the dominant species in the X-ray diffraction patterns from 298 K to 723 K. Diffraction peaks for γ -LaOF begin to show up in the patterns above 598 K. By 773 K, bastnäsite-(La) is no longer present in the patterns, and γ -LaOF is the only phase present. Above 948 K, only α -LaOF is present. γ -LaOF was the only species present in the pattern collected at 298 K after the sample was allowed to cool following the collection of the final high temperature pattern. β -LaOF was not evident in any of patterns. See Tables 1 to 3 for the measured lattice parameters and volumes of all three materials. Figures 6, 7, and 8 display measured unit cell volumes as a function of temperature for all three materials.

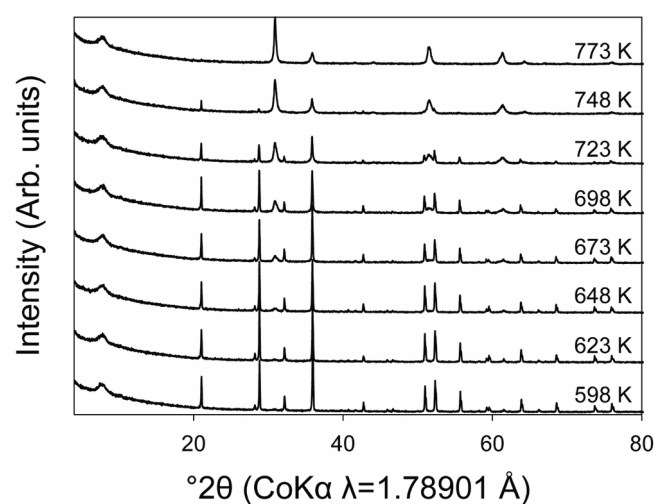


Figure 5: High temperature powder X-Ray diffraction patterns from 598 K to 723 K. Bottom pattern is 598 K, and the patterns go up in 25° temperature increments. Bottom-most pattern exhibits only bastnäsite-(La). Top-most pattern exhibits only γ -LaOF. The middle 6 patterns exhibit both species as the decomposition reaction progresses from bastnäsite-(La) to γ -LaOF.

Table 1 - Measured lattice parameters and volume for bastnäsite-(La) from 298 to 723 K.

Temperature (K)	a (Å)	Uncertainty y	c (Å)	Uncertainty	V (Å ³)	Uncertainty y	a/c ratio
	7.186						
298	7	0.00085	9.8328	0.00083	439.82	0.185	0.7309
	7.189						
323	7	0.00085	9.8347	0.00083	440.26	0.185	0.7311
	7.195						
373	4	0.00085	9.8394	0.00083	441.18	0.185	0.7313
	7.199						
423	2	0.00085	9.8438	0.00083	441.84	0.185	0.7313
473	7.204	0.00085	9.8486	0.00083	442.69	0.186	0.7315

	4						
	7.207						
498	4	0.00085	9.8504	0.00083	443.14	0.186	0.7317
	7.209						
523	6	0.00085	9.8539	0.00083	443.57	0.186	0.7316
	7.212						
548	5	0.00085	9.8564	0.00083	444.04	0.186	0.7318
	7.215						
573	9	0.00085	9.8572	0.00083	444.50	0.186	0.7320
	7.217						
598	2	0.00085	9.8598	0.00083	444.76	0.186	0.7320
	7.220						
623	5	0.00086	9.8626	0.00083	445.30	0.186	0.7321
	7.223						
648	8	0.00086	9.8669	0.00083	445.91	0.187	0.7321
	7.226						
673	6	0.00086	9.8669	0.00083	446.25	0.187	0.7324
	7.229						
698	6	0.00086	9.8730	0.00083	446.90	0.187	0.7323
	7.233						
723	9	0.00086	9.8731	0.00083	447.43	0.187	0.7327

Table 2 - Measured lattice parameters and volumes for γ -LaOF at 298 K, and from 723 K to 948 K.

Temperature (K)	a (Å)	Uncertainty y	c (Å)	Uncertainty y	V (Å ³)	Uncertainty y
	4.079					
298	8	0.00041	5.798	0.0020	96.51	0.118
	4.124					
723	2	0.00045	5.855	0.0030	99.59	0.130
	4.119					
748	2	0.00041	5.873	0.0020	99.65	0.119
	4.119					
773	2	0.00041	5.873	0.0020	99.65	0.119
	4.121					
798	3	0.00042	5.862	0.0020	99.57	0.119
	4.123					
823	0	0.00042	5.862	0.0020	99.64	0.119
	4.124					
848	6	0.00042	5.867	0.0020	99.80	0.119
	4.127					
873	6	0.00042	5.864	0.0020	99.91	0.119
	4.129					
898	3	0.00042	5.860	0.0020	99.92	0.119
	4.128					
923	6	0.00050	5.866	0.0022	99.99	0.122
	4.131				100.0	
948	1	0.00042	5.859	0.0020	0	0.119

222

223

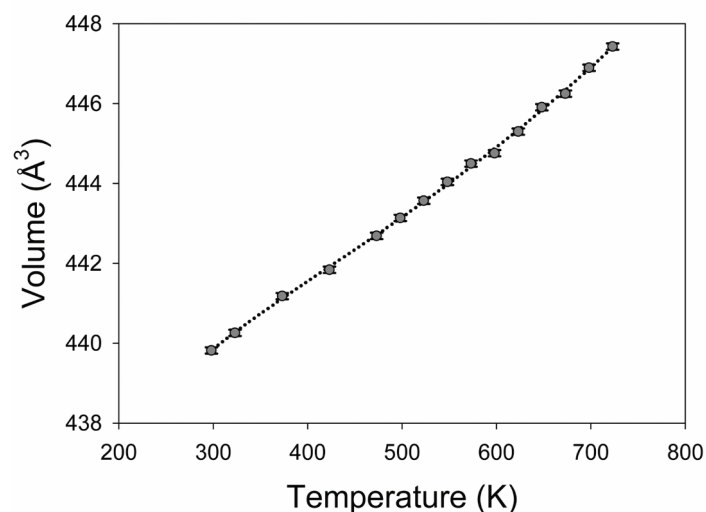
Table 3 - Measured lattice parameters and volumes for α -LaOF from 973 K to 1173 K.

Temperature (K)	a (Å)	Uncertainty y	V (Å ³)	Uncertainty y
	5.756		190.71	
298	*	0.003*	*	
	5.842			
973	4	0.00049	199.42	0.138
	5.844			
998	3	0.00049	199.62	0.138
	5.847			
1023	6	0.00050	199.95	0.138
	5.848			
1048	9	0.00050	200.08	0.138

	5.850			
1073	0	0.00050	200.20	0.138
	5.852			
1098	6	0.00050	200.47	0.138
	5.853			
1123	8	0.00050	200.60	0.138
	5.853			
1148	1	0.00050	200.52	0.138
	5.851			
1173	1	0.00050	200.32	0.138

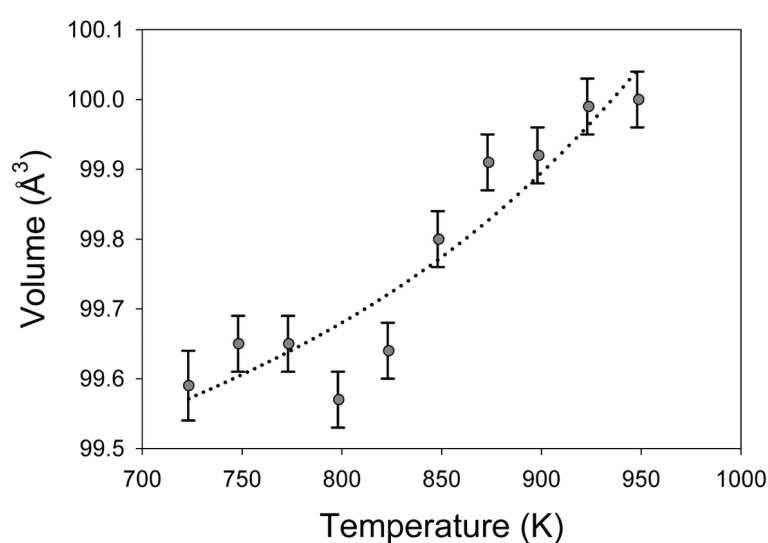
225 *values for ambient temperature (298 K) from [22] because this structure was not
226 recoverable to room temperature by quenching in the XRK-900 reactor stage.

227



228

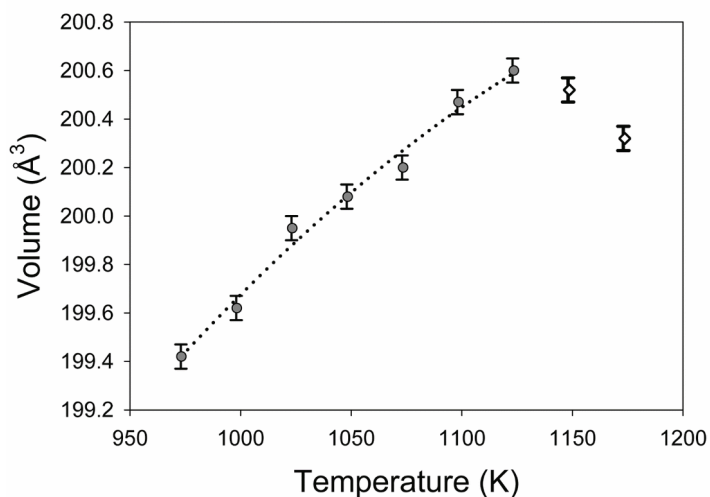
229 **Figure 6:** Measured unit cell volumes for bastnäsite-(La) as a function of temperature
 230 from 298 K to 723 K. The dotted black line is the fit for the Fei thermal equation of
 231 state [40].



232

233 **Figure 7:** Measured unit cell volumes for tetragonal γ -LaOF as a function of
 234 temperature from 723 K to 948 K. The dotted black line is the fit for the Fei thermal
 235 equation of state [40].

236

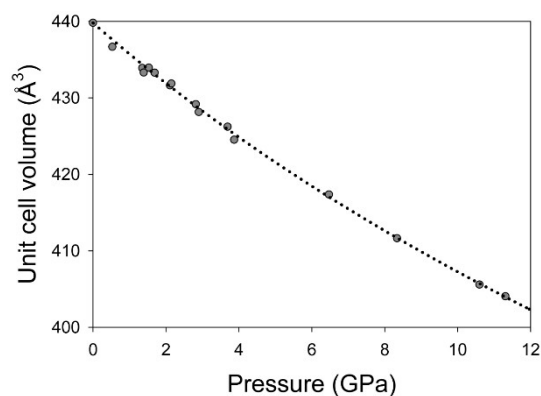


237

238 **Figure 8:** Measured unit cell volumes for cubic α -LaOF as a function of temperature
 239 from 973 K to 1123 K. Gray-filled circles represent data used to fit the thermal
 240 equation of state in this temperature range. White diamonds represent temperature
 241 points 1148 K and 1173 K which are above the temperature that coincides with a
 242 contraction in unit cell volume and an exotherm on the DSC curve. The dotted black
 243 line is the fit for the Fei thermal equation of state [40].

244 3.3 Single crystal X-ray diffraction

245 At ambient temperature, 16 X-ray diffraction patterns of bastnäsité-(La) were
 246 collected from ambient pressure to 11.3 GPa. Over this pressure range, the a -
 247 crystallographic axis contracts from 7.187 Å to 6.974 Å, the c - crystallographic axis
 248 contracts from 9.830 Å to 9.593 Å, with a corresponding unit cell volume contraction
 249 from 439.82 Å³ to 404.06 Å³. Table 4 lists the measured lattice parameters, calculated
 250 unit cell volumes, and crystallographic axis ratios for each pressure point. The unit
 251 cell volume data were fit to a third order Birch-Murnaghan equation of state [31,41]
 252 with $V_0 = 439.82$ Å³, $K_0 = 105$ GPa, and $K' = 5.58$. Figure 9 illustrates the unit cell
 253 volume measurements superimposed over the calculated equation of state.



254

255 **Figure 9:** Pressure-volume data measured for bastnäsité-(La) fit to the 3rd order
 256 Birch-Murnaghan equation of state [41]. $V_0 = 439.82$ Å³, $K_0 = 105$ GPa, $K' = 5.58$. Gray

circles are measured volumes from Table 4, dotted line represents equation of state fit to data.

Table 4: Bastnäs site-(La) measured lattice parameters, unit cell volumes, a/c crystallographic axis ratios, pressure transmitting media, and pressure standards from 0 to 11.3 GPa at ambient temperature.

Pressure (GPa)	a (Å)	Uncertainty	c (Å)	Uncertainty	V (Å ³)	Uncertainty	a/c ratio	Pressure media	Pressure standard
	7.18		9.83		439.8		0.730		
0.00	7	0.002	3	0.040	2	0.044	9	n/a	n/a
	7.16		9.81		436.6		0.730		
0.53	9	0.003	1	0.003	8	0.009	7	Ne	Au
	7.14		9.80		433.9		0.728		
1.35	8	0.003	6	0.003	1	0.008	9	Ne	Au
	7.15		9.76		433.3		0.733		
1.39	9	0.001	3	0.003	2	0.006	3	He	Cu
	7.15		9.78		433.9		0.731		
1.53	8	0.001	0	0.003	6	0.006	9	He	Cu
	7.15		9.78		433.3		0.730		
1.69	0	0.002	7	0.004	0	0.008	6	He	Cu
	7.14		9.76		431.6		0.731		
2.11	4	0.004	6	0.006	4	0.013	5	Ne	Au
	7.14		9.76		431.8		0.731		
2.15	5	0.001	9	0.003	8	0.005	4	He	Cu
	7.12		9.75		429.1		0.731		
2.82	9	0.001	1	0.003	8	0.005	1	He	Cu
	7.11		9.76		428.1		0.729		
2.90	7	0.002	1	0.002	5	0.006	1	Ne	Au
	7.11		9.73		426.2		0.730		
3.69	1	0.001	4	0.002	3	0.004	5	He	Cu
	7.09		9.73		424.5		0.728		
3.87	5	0.003	8	0.003	3	0.009	6	Ne	Au
	7.05		9.69		417.3		0.727		
6.47	1	0.003	4	0.003	8	0.009	4	Ne	Au
	7.01		9.66		411.6		0.725		
8.34	4	0.003	3	0.003	5	0.009	9	Ne	Au
	6.97		9.63		405.5		0.723		
10.60	3	0.003	2	0.003	9	0.009	9	Ne	Au
	6.97		9.59		404.0		0.727		
11.31	4	0.004	3	0.003	6	0.011	0	Ne	Au

Over the temperature range of 347 K to 673 K, nine X-ray diffraction patterns were collected between 4.9 GPa and 7.7 GPa. Over this range of conditions, the a -crystallographic axis varies between 7.057 Å and 7.086 Å, the c -crystallographic axis varies between 9.730 Å and 9.685 Å, with corresponding variation in unit cell volumes between 423.11 Å³ and 418.32 Å³. Table 5 lists the measured lattice parameters, calculated unit cell volumes, and crystallographic axis ratios for each pressure and temperature point.

Table 5: Bastnäsite-(La) measured lattice parameters, unit cell volumes, and a/c crystallographic axis ratios from 4.9 to 7.7 GPa pressure and from 347 K to 673 K temperature.

Pressure (GPa)	Temperature (K)	a (Å)	Uncertainty	c (Å)	Uncertainty	V (Å ³)	Uncertainty	a/c ratio
		7.08		9.73		423.1		0.728
4.9	347	6	0.001	0	0.002	1	0.005	3
		7.08		9.72		422.4		0.728
5.1	324	4	0.002	1	0.002	7	0.006	7
		7.07		9.69		420.4		0.729
5.8	373	6	0.002	6	0.002	4	0.006	8
		7.07		9.69		419.8		0.728
6.5	423	0	0.002	9	0.003	5	0.007	9
		7.06		9.69		418.3		0.728
6.7	473	0	0.002	1	0.002	2	0.006	5
		7.06		9.69		418.9		0.728
6.7	523	3	0.002	7	0.003	3	0.007	4
		7.05		9.71		418.9		0.726
7.0	573	7	0.002	3	0.003	1	0.007	6
		7.06		9.69		419.0		0.728
7.3	623	5	0.001	4	0.002	1	0.005	8
		7.06		9.68		418.5		0.729
7.7	673	4	0.002	5	0.002	3	0.006	4

4. Discussion

From TGA/DSC and high temperature powder XRD data, it is apparent that at ambient pressure, the decarbonation temperature of bastnäsite-(La) is about 598 K. Above this temperature, the decomposition reaction of bastnäsite-(La) into γ -LaOF and CO₂ begins. Since our experiments were conducted without controlled pCO₂, this decarbonation point is not necessarily the equilibrium decomposition temperature. The application of pressure significantly increases the stability of bastnäsite-(La) as was observed in our recrystallization experiments at 1073 K and 0.22 GPa (after 5 hours) and at 1123 K and 0.71 GPa after 21 hours [28]. However, as these experiments were not reversed, a phase diagram for bastnäsite-(La) cannot yet be

established. At 948 K, tetragonal γ -LaOF undergoes a first order structural phase transition reaction to cubic α -LaOF. The decomposition temperature for bastnäsité-(La) found in this study agrees with previous values reported by Janka and Schlied [15] who used similar methods, but did not report behavior for temperatures above 823 K. While the sample material cooled back down to 298 K, it transformed to γ -LaOF, the stable structure of lanthanum oxyfluoride at ambient conditions.

Table 6 lists the fitted thermal expansion coefficients for bastnäsité-(La), γ -LaOF, and α -LaOF over the temperature ranges measured in the high temperature powder X-ray diffraction experiments. Over the temperature ranges measured, all three species exhibit a trend of positive thermal expansion (Figures 6, 7, and 8) except between 1123 K and 1173 K, where the α -LaOF unit cell contracts. There is an endotherm in the DSC curve at 1123 K that could indicate a phase transition, but the X-ray diffraction patterns at these temperatures do not indicate a structural change, and the mass spectrometer did not detect any compounds outgassing at these temperatures; further studies are necessary to determine what this endotherm and coincident thermal contraction represent.

Table 6: Calculated thermal expansion coefficients for bastnäsité-(La), γ -LaOF, and α -LaOF.

Material		Temp. Range (K)	α_{298} $\times 10^{-5}$	a_0 $\times 10^{-5}$	a_1 $\times 10^{-7}$	a_2
bastnäsité-(La)	$a(a_0=7.1867 \text{ Å})$	298-723	1.73	-1.08	0.373	1.502
	$c(c_0=9.8328 \text{ Å})$	298-723	0.951	0.247	0.116	0.319
	$V(V_0=439.82 \text{ Å}^3)$	298-723	4.32	-1.68	0.834	3.126
γ -LaOF	$a(a_0=4.0798 \text{ Å})$	723-948	13.5	-17.9	1.90	22.879
	$c(c_0=5.798 \text{ Å})$	723-948	0.179	0.1785	-0.229	8.154
	$V(V_0=96.51 \text{ Å}^3)$	723-948	29.5	-24.1	2.42	41.147
α -LaOF	$a(a_0=5.756 \text{ Å})$	973-1123	-0.844	8.46	-0.625	-6.606
	$V(V_0=190.71 \text{ Å}^3)$	973-1123	-1.12	23.6	-1.73	-17.362

Note: Reference temperature for all fits is 298 K.

Thermal analysis has not been performed on any other fluorocarbonate minerals, so a direct comparison of the properties of bastnäsité-(La) measured in this investigation to other materials with similar structure is not possible. Others have investigated the thermal expansion of more common carbonates including aragonite (CaCO_3), strontianite (SrCO_3), cerrusite (PbCO_3), witherite (BaCO_3) [42], calcite (CaCO_3), and magnesite (MgCO_3) [43]. A comparison of the thermal equations of state for bastnäsité-(La) and these materials is given in Figure 10. Compared with these more common carbonates, bastnäsité-(La) experiences more thermal expansion for a given increase in temperature than the trigonal R-3c carbonates (calcite and magnesite), and less thermal expansion for a given increase in temperature than the orthorhombic Pmcn carbonates (aragonite, cerrusite, strontianite, and witherite). Also of note, as shown in Table 6, bastnäsité-(La)'s *a*- and *c*- crystallographic axes expand

at different rates; all of the other carbonates listed above also exhibit some degree of anisotropic thermal expansion. Overall, this indicates that bastnäsite-(La)'s thermal expansion behavior is similar to that of other carbonate minerals.

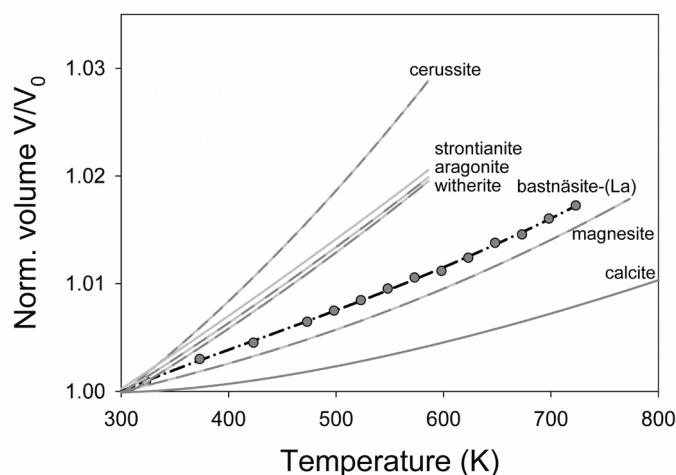


Figure 10: Comparisons of ambient pressure thermal equations of state for different carbonate minerals. Gray circles represent bastnäsite-(La) data from this study, and the dotted black line represent the fitted Fei equation of state [40] for bastnäsite-(La). Thermal equations of state are shown for calcite (CaCO_3), magnesite (MgCO_3) [43], witherite (BaCO_3), cerrusite (PbCO_3), strontianite (SrCO_3), and aragonite (CaCO_3) [42].

There are no previous studies of tetragonal REE-bearing oxyfluorides, but Achary et al. [24] synthesized the rhombohedral oxyfluorides of five REE's (La, Nd, Sm, Eu, and Gd), and used high temperature powder XRD to investigate their thermal expansion and phase transformation to cubic structures at high temperature. Their calculation and fitting of thermal expansion coefficients used the data for both rhombohedral and cubic phases, so the resulting thermal equations of state are not suitable to compare directly to that for α -LaOF derived in this study. However, using their data for just the cubic phases, we were able to fit thermal expansion coefficients using EOSFit7GUI [31]. Table 7 lists the fitted coefficients, and Figure 11 illustrates the thermal equations of state compared to that of α -LaOF measured in this study. The thermal expansion behavior we measured for α -LaOF is essentially the same as what we derive from Achary et al.'s data [24].

340 **Table 7: Calculated thermal expansion coefficients for cubic REE-oxyfluorides.**

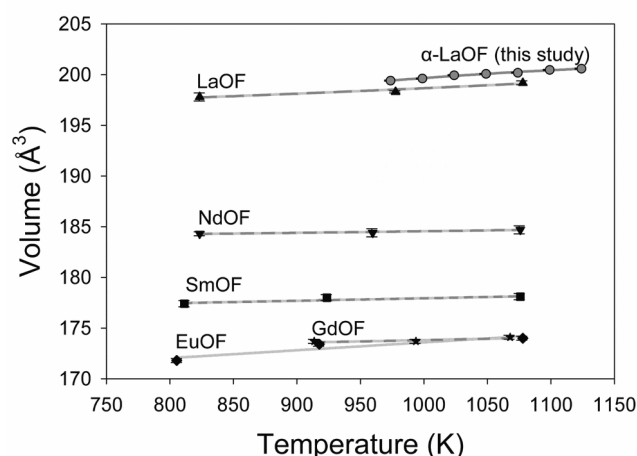
Material	Temp. Range (K)	V_o (\AA^3)	α_{298} $\times 10^{-5}$	a_o $\times 10^{-5}$	a_1 $\times 10^{-7}$	a_2
α -LaOF†	973-1123	190.71	-1.12	23.6	-1.73	-17.362
α -LaOF *	823-1077	196.1	0.855	0.0017	0.286	0.0001
NdOF*	823-1075	183.8	0.268	0.0007	0.0895	0.0001
SmOF*	811-1075	176.2	1.4	1.4	0.00028	0
EuOF*	815-1077	168.2	4.49	4.49	0.00052	0.0001
GdOF*	913-1067	172.6	0.461	0.0044	0.1530	0

341 Note: Reference temperature for all fits is 298 K.

342 † this study

343 * data from Achary, et. al [24].

344



345

346 **Figure 11:** Comparisons of ambient pressure thermal equations of state for cubic
 347 REE-OF compounds from this study and using data from Achary et al. [24] (solid
 348 symbols). Gray circles are data for cubic α -LaOF from this study.

349

350 The anisotropy of bastnäsite-(La) is enhanced under compression; the a -
 351 crystallographic axis contracts more than the c - crystallographic axis. The changing
 352 ratio of a/c is given in Table 4. Similarly, the a - crystallographic axis is also more
 353 expansive during heating (Table 1). As illustrated in Figure 1, the planar carbonate
 354 ions are arranged in the structure such that they lie on planes containing the c -
 355 crystallographic axis. Others [44–46] have observed rigid body behavior of CO_3^{2-}
 356 anions in other carbonates at high pressure. Thus, we suggest that most of the
 357 expansion and contraction of the structure is accommodated by the La-O and La-F
 358 bonds.

359 There are no compressibility data fit to equations of state or any bulk moduli
 360 measured from other methods (e.g., ultrasonic methods) in the literature for

bastnäsite or any other fluorocarbonate minerals, so a direct comparison of the properties of bastnäsite-(La) measured in this investigation to materials with similar structure is not possible. However, our results are consistent with recent work on natural materials that shows that the bastnäsite structure is stable up to 25 GPa at room temperature [47]. Anderson and Nafe [48] found that when comparing many compounds' bulk moduli versus their specific ionic volumes, multiple trends emerged. Figure 12 displays their data, with additional data for carbonate minerals from Knittle [49], Merlini [50], and Xu [51]. Anderson and Nafe [48] identified a sulfide-selenide-telluride trend, an oxide trend, a fluorite trend, and an alkali-halide trend. Rhodochrosite, dolomite, ankerite, calcite, strontianite, and witherite form a separate carbonate trend (yellow line in Figure 12), but the hydroxycarbonates azurite and malachite do not lie on this trend. The values measured for bastnäsite-(La) in this study plot in a location consistent with the carbonate trend, the fluorite trend, as well as the oxide trend. Work on other fluorocarbonates needs to be completed in order to determine which of these trends bastnäsites follow, or if fluorocarbonates have a separate trend. If the speculation above that bastnäsite-(La)'s compressional anisotropy is related to rigid body behavior and orientation of the carbonate ions is correct, it is then likely that bastnäsites would follow the carbonate trend.

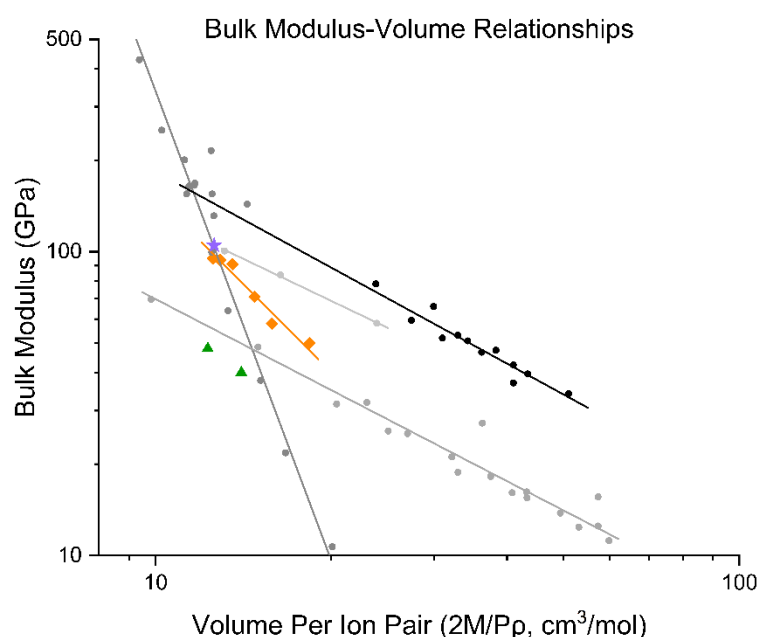


Figure 12: Bulk modulus versus specific volume for simple oxides, alkali halides, fluorites, sulfides, selenides, tellurides, and carbonates. Small circles include data from [48] and [49]. Large purple star is the value for bastnäsite-(La) measured in this study ($2M/Pp = 12.60 \text{ cm}^3/\text{mol}$, $K_0 = 105 \text{ GPa}$), large orange diamonds are carbonates from [49], and green triangles are malachite and azurite from [50,51]. Dark gray line is the oxide trend, black line is the sulfide, selenide, and telluride trend, light gray line is the fluorite trend, medium gray line is the alkali-halide trend, and orange line is proposed carbonate trend.

While some of our measurements were taken at elevated temperature and pressure (Table 5), there is not enough data to properly fit a high temperature and pressure equation of state. However, these data can be used to evaluate whether our isothermal and thermal equations of state can be combined to predict bastnäsit-(La)'s unit cell volume at high temperature and pressure. Thus for each pressure, temperature point measured in our heated DAC experiments we calculated the value for V_0 (at $P=0$) using our values for the thermal equation of state [40], and then used our Birch-Murnaghan equation of state [41] to calculate the pressure required to produce the observed unit cell volume. The pressures calculated in this way agree well with those measured from the copper pressure standard. Table 8 lists the measured temperatures, unit cell volumes, and pressures, and the calculated pressures. Since the temperatures and volumes from the elevated temperature DAC experiments were not used in the fitting of Fei's thermal equation of state or in the fitting of the Birch-Murnaghan equation of state, these data show that the combination of both equations is a reasonable approximation for modeling changes in volume due to both pressure and temperature simultaneously.

Table 8: List of heated DAC experiments comparing measured pressure using the Cu standard versus calculated pressures using the Fei thermal EOS [40] parameters. Difference is calculated by subtracting the measured pressure from the calculated pressure. Error is calculated by dividing the difference by the measured pressure.

Temp (K)	V (\AA^3)	Measured P (GPa)	Calculated P (GPa)	Differenc e	Erro r
	423.1				
347	1	4.90	5.03	0.13	0.03
	422.4				
324	7	5.09	5.11	0.02	0.00
	420.4				
373	4	5.78	6.02	0.24	0.04
	419.8				
423	5	6.46	6.46	0.00	0.00
	418.3				
473	2	6.74	7.23	0.49	0.07
	418.9				
523	3	6.71	7.28	0.57	0.08
	418.9				
573	1	6.97	7.57	0.60	0.09
	419.0				
623	1	7.33	7.84	0.51	0.07
	418.5				
673	3	7.69	8.33	0.64	0.08

412 **5. Conclusions**

413 Compressibility, thermal expansion and phase stability are fundamental
414 thermodynamic properties of materials, and as such are significant in understanding
415 how they interact with the geologic settings in which the minerals naturally occur.
416 Bastnäs site-La and the lanthanum oxyfluoride polymorphs addressed above are
417 important REE-bearing compounds, and thus studying them is useful for
418 understanding how REE bearing compounds form and participate in chemical
419 reactions with other compounds. Additionally, since bastnäs site is found in
420 carbonatites, it is an important mineral to investigate in order to understand
421 carbonated magmas and the formation of carbonatite-related ore deposits. Gaining
422 insight to the thermodynamic behavior of bastnäs site and other fluorocarbonates could
423 potentially lead to better methods of locating and processing REE ore in the future.

424

Author Contributions: Conceptualization, R.R., P.C.B. and B.L. ; methodology, R.R., B.L., K.E.V.K.; formal analysis, R.R. and B.L.; investigation, R.R.; resources, P.C.B. and L.D.; data curation, P.C.B.; writing—original draft preparation, R.R.; writing—review and editing, P.C.B., L.D., and K.E.V.K.; supervision, P.C.B.; project administration, P.C.B.; funding acquisition, P.C.B. All authors have read and agreed to the published version of the manuscript.

Funding: This research was sponsored in part by the National Nuclear Security Administration under the Stewardship Science Academic Alliances program through DOE Cooperative Agreement #DE-NA0001982 as well as by National Science Foundation grant EAR-1220548.

Acknowledgments: The high pressure work was conducted at HPCAT (Sector 16), Advanced Photon Source (APS), Argonne National Laboratory. HPCAT operations are supported by DOE-NNSA's Office of Experimental Sciences. The Advanced Photon Source, a U.S. Department of Energy (DOE) Office of Science User Facility operated for the DOE Office of Science by Argonne National Laboratory under Contract No. DE-AC02-06CH11357. Use of the COMPRES-GSECARS gas loading system was supported by COMPRES under NSF Cooperative Agreement EAR 11-57758 and by GSECARS through NSF grant EAR-1128799 and DOE grant DE-FG02-94ER1466. We thank Sergey Tkachev for his assistance with the gas loadings. This research also used resources and equipment at the National Aeronautics and Space Administration Lyndon B. Johnson Space Center's Astromaterials Research and Exploration Science division. We thank Brad Sutter of Jacobs JETS at NASA Johnson Space Center for assistance with the high temperature powder XRD data collection and Joanna V. Hogancamp of Geocontrols Systems and Jacobs JETS at NASA Johnson Space Center for assistance with TGA, DSC, and EGA data collection. The authors also wish to thank several anonymous reviewers for helpful suggestions.

Conflicts of Interest: The authors declare no conflict of interest. The funders had no role in the design of the study; in the collection, analyses, or interpretation of data; in the writing of the manuscript, or in the decision to publish the results.

References

1. Chen, Z. Global rare earth resources and scenarios of future rare earth industry. *J. Rare Earths* **2011**, *29*, 1–6.
2. Long, K.R.; Van Gosen, B.S.; Foley, N.K.; Cordier, D. The Principal Rare Earth Elements Deposits of the United States: A Summary of Domestic Deposits and a Global Perspective. *US Geol. Surv. Sci. Investig.* **2010**, *2010*, 96.
3. Workman, R.K.; Hart, S.R. Major and trace element composition of the depleted MORB mantle (DMM). *Earth Planet. Sci. Lett.* **2005**, *231*, 53–72.
4. Ni, Y.; Hughes, J.M.; Mariano, A.N. The atomic arrangement of bastnäsite-(Ce), Ce(CO₃)F, and structural elements of synchysite-(Ce), röntgenite-(Ce), and parisite-(Ce). *Am. Mineral.* **1993**, *78*, 415–418.
5. Olson, J.C.; Shawe, D.R.; Pray, L.C.; Sharp, W.N.; Hewett, D.F. Rare-Earth Mineral Deposits of the Mountain Pass District San Bernardino County California. *Geol. Surv. Prof. Pap.* **1954**, *261*, 4–15.
6. Williams-Jones, A.E.; Wood, S.A. A preliminary petrogenetic grid for REE fluorocarbonates and associated minerals. *Geochim. Cosmochim. Acta* **1992**,

- 470 56, 725–738.
- 471 7. Hsu, L.C. Synthesis and Stability of Bastnaesites in a Part of the System (Ce,La)-
472 F-H-C-O. *Mineral. Petrol.* **1992**, *47*, 87–101.
- 473 8. Schmandt, D.S.; Cook, N.J.; Ciobanu, C.L.; Ehrig, K.; Wade, B.P.; Gilbert, S.;
474 Kamenetsky, V.S. Rare earth element fluorocarbonate minerals from the
475 olympic dam Cu-U-Au-Ag deposit, South Australia. *Minerals* **2017**, *7*.
- 476 9. Oftedal, I. Zur Kristallstruktur von Bastnäsit, (Ce,La--) FCO_3 . *Zeitschrift für*
477 *Krist. Krist. Krist. Krist.* **1931**, *78*, 462.
- 478 10. Donnay, G.; Donnay, J.D.H. The Crystallography of Bastnaesite, Parisite,
479 Roentgenite, and Synchisite. *Am. Mineral.* **1953**, *38*, 932–963.
- 480 11. Castor, S.B. Rare Earth Deposits of North America. *Resour. Geol.* **2008**, *58*,
481 337–347.
- 482 12. Castor, S.B. The Mountain Pass Rare-Earth Carbonatite and Associated
483 Ultrapotassic Rocks, California. *Can. Mineral.* **2008**, *46*, 779–806.
- 484 13. Shivaramaiah, R.; Anderko, A.; Riman, R.E.; Navrotsky, A. Thermodynamics of
485 bastnaesite: A major rare earth ore mineral. *Am. Mineral.* **2016**, *101*, 1129–
486 1134.
- 487 14. Gysi, A.P.; Williams-Jones, A.E. The thermodynamic properties of bastnäsit-
488 (Ce) and parisite-(Ce). *Chem. Geol.* **2015**, *392*, 87–101.
- 489 15. Janka, O.; Schleid, T. Facile Synthesis of Bastnaesite-Type $\text{LaF}[\text{CO}_3]$ and Its
490 Thermal Decomposition to LaOF for Bulk and Eu^{3+} -Doped Samples. *Eur. J.*
491 *Inorg. Chem.* **2009**, *2009*, 357–362.
- 492 16. Woo, D.C.; Lee, M.-H.; Jung, W.-S. Synthesis and characterization of
493 rhombohedral- and tetragonal-lanthanum oxyfluoride powders. *Ceram. Int.*
494 **2013**, *39*, 1533–1538.
- 495 17. Jacob, K.T.; Saji, V.S.; Waseda, Y. Lanthanum Oxyfluoride: Structure, Stability,
496 and Ionic Conductivity. *Int. J. Appl. Ceram. Technol.* **2006**, *3*, 312–321.
- 497 18. Fergus, J.W.; Chen, H.-P. Structure and Conductivity of Tetragonal and
498 Rhombohedral Lanthanum Oxyfluoride Compounds. *J. Electrochem. Soc.* **2000**,
499 *147*, 4696–4704.
- 500 19. Shinn, D.B.; Eick, H.A. Phase Analyses of Lanthanide Oxide Fluorides. *Inorg.*
501 *Chem.* **1969**, *8*, 232–235.
- 502 20. Zachariasen, W.H. Crystal Chemical Studies of the 5f-series of Elements. XIV.
503 Oxyfluorides, XOF. *Acta Crystallogr.* **1951**, *4*, 231–236.
- 504 21. Pistorius, C.W.F.T. Effect of Pressure on the Rhombohedral/Cubic Transitions of
505 Some Lanthanide Oxide Fluorides. *J. Less-Common Met.* **1973**, *31*, 119–124.
- 506 22. Klemm, V.W.; Klein, H.-A. Lanthanoxyfluorid [Lanthanum Oxyfluoride].
507 *Zeitschrift für Anorg. und Allg. Chemie (in Ger.)* **1941**, *248*, 167–171.
- 508 23. Mathews, M.D.; Tyagi, A.K.; Moorthy, P.N. Study of phase transition in REOF
509 system by dilatometry (RE = La, Nd, Sm, Gd, Eu and Y). *Thermochim. Acta*
510 **1997**, *298*, 165–167.
- 511 24. Achary, S.N.; Ambekar, B.R.; Mathews, M.D.; Tyagi, A.K.; Moorthy, P.N. Study
512 of phase transition and volume thermal expansion in a rare-earth (RE)
513 oxyfluoride system by high-temperature XRD (RE=La, Nd, Sm, Eu and Gd).

- 514 *Thermochim. Acta* **1998**, *320*, 239–243.
- 515 25. Holtstam, D.; Grins, J.; Nysten, P. Håleniusite- (La) from the Bastnäs Deposit,
516 Västmandland, Sweden: A new REE Oxyfluoride Mineral Species. *Can. Mineral.*
517 **2004**, *42*, 1097–1103.
- 518 26. Momma, K.; Izumi, F. VESTA 3 for three-dimensional visualization of crystal,
519 volumetric and morphology data. *J. Appl. Crystallogr.* **2011**, *44*, 1272–1276.
- 520 27. Tullis, T.E.; Tullis, J. Experimental Rock Deformation Techniques. *Geophys.*
521 *Monogr.* **1986**, *36*, 297–324.
- 522 28. Rowland II, R.L. Phase Equilibria, Compressibility, and Thermal Analysis of
523 Bastnaesite-(La), University of Nevada, Las Vegas, 2017.
- 524 29. Altomare, A.; Corriero, N.; Cuocci, C.; Falcicchio, A.; Moliterni, A.; Rizzi, R.
525 QUALX2.0: a qualitative phase analysis software using the freely available
526 database POW_COD. *J. Appl. Crystallogr.* **2015**, *48*, 598–603.
- 527 30. Holland, T.J.B.; Redfern, S.A.T. Unit cell refinement from powder diffraction
528 data: the use of regression diagnostics. *Mineral. Mag.* **1997**, *61*, 65–77.
- 529 31. Angel, R.J.; Gonzalez-Platas, J.; Alvaro, M. EosFit7c and a Fortran module
530 (library) for equation of state calculations. *Zeitschrift fur Krist.* **2014**, *229*, 405–
531 419.
- 532 32. Kantor, I.; Prakapenka, V.; Kantor, A.; Dera, P.; Kurnosov, A.; Sinogeikin, S.;
533 Dubrovinskaia, N.; Dubrovinsky, L. BX90: A new diamond anvil cell design for X-
534 ray diffraction and optical measurements. *Rev. Sci. Instrum.* **2012**, *83*.
- 535 33. Hrubiak, R.; Sinogeikin, S.; Rod, E.; Shen, G. The laser micro-machining system
536 for diamond anvil cell experiments and general precision machining
537 applications at the High Pressure Collaborative Access Team. *Rev. Sci. Instrum.*
538 **2015**, *86*.
- 539 34. Rivers, M.; Prakapenka, V.B.; Kubo, A.; Pullins, C.; Holl, C.M.; Jacobsen, S.D.
540 The COMPRES/GSECARS gas-loading system for diamond anvil cells at the
541 Advanced Photon Source. *High Press. Res.* **2008**, *28*, 273–292.
- 542 35. Mao, H.K.; Xu, J.; Bell, P.M. Calibration of the Ruby Pressure Gauge to 800 kbar
543 Under Quasi-Hydrostatic Conditions. *J. Geophys. Res.* **1986**, *91*, 4673.
- 544 36. Hirose, K.; Sata, N.; Komabayashi, T.; Ohishi, Y. Simultaneous volume
545 measurements of Au and MgO to 140 GPa and thermal equation of state of Au
546 based on the MgO pressure scale. *Phys. Earth Planet. Inter.* **2008**, *167*, 149–
547 154.
- 548 37. Wang, Y.; Zhang, J.; Xu, H.; Lin, Z.; Daemen, L.L.; Zhao, Y.; Wang, L. Thermal
549 equation of state of copper studied by high P-T synchrotron x-ray diffraction.
550 *Appl. Phys. Lett.* **2009**, *94*, 4.
- 551 38. Hammersley, A.P. FIT2D: A multi-purpose data reduction, analysis and
552 visualization program. *J. Appl. Crystallogr.* **2016**, *49*, 646–652.
- 553 39. Dera, P.; Zhuravlev, K.; Prakapenka, V.; Rivers, M.L.; Finkelstein, G.J.; Grubor-
554 Urosevic, O.; Tschauner, O.; Clark, S.M.; Downs, R.T. High pressure single-
555 crystal micro X-ray diffraction analysis with GSE_ADA/RSV software. *High*
556 *Press. Res.* **2013**, *33*, 466–484.
- 557 40. Fei, Y. Thermal Expansion. In *Mineral Physics and Crystallography: A Handbook*

of *Physical Constants*; Ahrens, T.J., Ed.; American Geophysical Union: Washington, DC 20009, 1995; pp. 29–44 ISBN 0-87590-852-7.

41. Birch, F. Finite Elastic Strain of Cubic Crystals. *Phys. Rev.* **1947**, *71*, 809–824.
42. Ye, Y.; Smyth, J.R.; Boni, P. Crystal structure and thermal expansion of aragonite-group carbonates by single-crystal X-ray diffraction. *Am. Mineral.* **2012**, *97*, 707–712.
43. Markgraf, S.A.; Reeder, R.J. High-temperature structure refinements of calcite and magnesite. *Am. Mineral.* **1985**, *70*, 590–600.
44. Ross, N.L.; Reeder, R.J. High-pressure structural study of dolomite and ankerite. *Am. Mineral.* **1992**, *77*, 412–421.
45. Ross, N.L. The equation of state and high-pressure behavior of magnesite. *Am. Mineral.* **1997**, *82*, 682–688.
46. Zhang, J.; Reeder, R.J. Comparative compressibilities of calcite-structure carbonates: Deviations from empirical relations. *Am. Mineral.* **1999**, *84*, 861–870.
47. Vennari, C.E.; Williams, Q. High-pressure Raman and Nd³⁺ luminescence spectroscopy of bastnäsite-(REE)CO₃F. *Am. Mineral.* **2019**, *104*, 1389–1401.
48. Anderson, O.L.; Nafe, J.E. The Bulk Modulus-Volume Relationship for Oxide Compounds and Related Geophysical Problems. *J. Geophys. Res.* **1965**, *70*, 3951–3963.
49. Knittle, E. Static Compression Measurements of Equation of State. In *Mineral physics and crystallography: a handbook of physical constants*; Ahrens, T.A., Ed.; American Geophysical Union, 1995; pp. 98–142.
50. Merlini, M.; Perchiazzi, N.; Hanfland, M.; Bossak, A. Phase transition at high pressure in Cu₂CO₃(OH)₂ related to the reduction of the Jahn-Teller effect. *Acta Crystallogr. Sect. B Struct. Sci.* **2012**, *B68*, 266–274.
51. Xu, J.; Kuang, Y.; Zhang, B.; Liu, Y.; Fan, D.; Zhou, W.; Xie, H. High-pressure study of azurite Cu₃(CO₃)₂(OH)₂ by synchrotron radiation X-ray diffraction and Raman spectroscopy. *Phys. Chem. Miner.* **2015**, *42*, 805–816.



© 2020 by the authors. Submitted for possible open access publication under the terms and conditions of the Creative Commons Attribution (CC BY) license (<http://creativecommons.org/licenses/by/4.0/>).